

## RESEARCH ARTICLE

# Single STE-MR Acquisition in MR-Based Attenuation Correction of Brain PET Imaging Employing a Fully Automated and Reproducible Level-Set Segmentation Approach

Anahita Fathi Kazerooni,<sup>1,2</sup> Mohammad Reza Ay,<sup>2,3</sup> Saman Arfaie,<sup>4</sup> Parisa Khateri,<sup>3</sup> Hamidreza Saligheh Rad<sup>1,2</sup>

<sup>1</sup>Quantitative MR Imaging and Spectroscopy Group (QMISG), Research Center for Molecular and Cellular Imaging (RCMCI), Tehran University of Medical Sciences, Tehran, Iran

<sup>2</sup>Department of Medical Physics and Biomedical Engineering, Tehran University of Medical Sciences, Tehran, Iran

<sup>3</sup>Medical Imaging Systems Group (MISG), Research Center for Molecular and Cellular Imaging (RCMCI), Tehran University of Medical Sciences, Tehran, Iran

<sup>4</sup>College of Letters and Science, Department of Molecular and Cell Biology, University of California, Berkeley, USA

### Abstract

**Purpose:** The aim of this study is to introduce a fully automatic and reproducible short echo-time (STE) magnetic resonance imaging (MRI) segmentation approach for MR-based attenuation correction of positron emission tomography (PET) data in head region.

**Procedures:** Single STE-MR imaging was followed by generating attenuation correction maps ( $\mu$ -maps) through exploiting an automated clustering-based level-set segmentation approach to classify head images into three regions of cortical bone, air, and soft tissue. Quantitative assessment was performed by comparing the STE-derived region classes with the corresponding regions extracted from X-ray computed tomography (CT) images.

**Results:** The proposed segmentation method returned accuracy and specificity values of over 90 % for cortical bone, air, and soft tissue regions. The MR- and CT-derived  $\mu$ -maps were compared by quantitative histogram analysis.

**Conclusions:** The results suggest that the proposed automated segmentation approach can reliably discriminate bony structures from the proximal air and soft tissue in single STE-MR images, which is suitable for generating MR-based  $\mu$ -maps for attenuation correction of PET data.

**Key words:** PET/MRI, Attenuation correction, Attenuation map, STE-MRI, Level-set technique

## Introduction

Attenuation correction is a mandatory step for exploiting both qualitative and quantitative capabilities of positron

emission tomography (PET) images and to achieve desirable diagnostic accuracy [1]. In this context, magnetic resonance imaging (MRI) has recently emerged as a potential substitute for computed tomography (CT) imaging in providing accurate quantitative attenuation correction map ( $\mu$ -map) of radiotracer concentration, due to the significant advantages it offers over CT imaging [2, 3]. As opposed to conventionally used CT images for generating PET attenuation correction, MRI delivers high-resolution and high-contrast images [4]. Additionally, the metabolic information provided by PET

Electronic supplementary material The online version of this article (doi:10.1007/s11307-016-0990-5) contains supplementary material, which is available to authorized users.

Correspondence to: Hamidreza Saligheh Rad; e-mail: h-salighehrad@tums.ac.ir

could be complemented by additional functional MRI techniques, e.g., spectroscopy, perfusion, and diffusion, which can be carried out without imposing any radiation dose and in the same imaging session with routine MRI [4, 5].

Incorporating MRI with PET scanning has now become a reality in hybrid PET/MR scanners, in which simultaneous image acquisition can reduce the overall acquisition time. Hybrid PET/MRI allow for establishing correlations among MRI-based morphological and functional information with PET-based pathological and quantitative information on metabolic aspects of tissue function [6].

Nonetheless, one of the main challenges currently being faced in PET/MRI systems is the difficulty to directly generate  $\mu$ -maps at 511 keV by the corresponding MRI; mostly because, there are no direct interrelationships between MRI intensities and attenuation coefficients of the tissue [6, 7]. Nonetheless, an issue with MRI-based attenuation correction (MRAC) is that in conventional MRI, cortical bone structures are indistinguishable from proximal air cavities, e.g., in facial sinuses in the head images [8]. Since air and bone manifest different attenuation properties, misclassification of bony structures as air or soft tissue classes could lead to errors as large as 20 % in estimation of radiotracer concentration [7, 9, 10]. Hence, accurate tissue segmentation becomes critically important in deriving quantitative PET images.

To reliably create MRI-derived  $\mu$ -maps at 511 keV, template- [11, 12], segmentation- [8, 13], and sequence-based [7, 13, 14] methods have been proposed. The template-based approaches predict the attenuation coefficients on a continuous scale, usually by either registering a CT atlas or PET transmission scan template or through applying machine learning techniques [15, 16]. But, these approaches are time-consuming, cannot perform optimally in presence of pathologies, and their robustness to anatomical variability among different subjects must be carefully evaluated. In other words, these techniques do not account for inter-patient variability. The segmentation-based methods that works purely based on MR images, acquired by properly-designed pulse sequences such as ultra-short echo-time (UTE) or short echo-time (STE) techniques, are generally simpler to implement, computationally efficient, and relatively robust.

While UTE-MRI that detects the bone signal and thus facilitates discrimination of cortical bone from air, has received attention for MRAC of PET images in the past few years [13, 17], it has a number of limitations which restrict its application in routine clinical imaging: UTE-MRI is time-consuming, requires two sequential imaging acquisitions, and yet delineating borders of air, cortical bone, and soft tissue is a challenge [6]. Recently, we investigated the feasibility of STE-MRI, a widely available and cost-effective sequence, in the head area as an alternative to UTE-MRI and showed its potential in differentiating cortical bone from air [14, 18].

STE-MRI provides sufficient cortical bone signal for its differentiation from air but appears with discontinuous boundaries, and this complicates the performances of intensity-based segmentation techniques, such as thresholding [18] or fuzzy C-means [14] in discontinuities. In such occasions, manipulations with morphological operators are required to attach the missing parts for generating homogeneous cortical bone regions, and therefore, the ultimate approach becomes semi-automated and dependent on the judgment of the algorithm developer, which is not reproducible. The presence of intensity inhomogeneity artifacts can further degrade the performances of such algorithms, as the signal intensities become interrelated in adjacent pixels while the assumption of aforementioned segmentation techniques is independent of image pixels.

Our previous work incorporated combination of STE and Dixon imaging for discrimination of tissue classes, which requires additional imaging. In the present study, we intended to design and implement an efficient segmentation scheme employing fully automatic and reproducible level-set segmentation approach on single STE-MRI, to reliably discriminate the cortical bone from soft tissue and air in the head region.

## Materials and Methods

### Image Acquisition

Study approval was obtained from the Medical Ethics Committee of Tehran University of Medical Sciences (License number 1432), and the subjects were included if they provided written informed consent. MR image acquisitions of five volunteers were performed on a 1.5 T MAGNETOM Avanto system (Siemens Medical Solutions, Erlangen, Germany). Short TE (STE)-MR images were acquired using FLASH 3D pulse sequence with the following parameters (summarized in Table 1): TE/TR of 1.13/12 ms, flip angle of 18°, and voxel size of  $1.2 \times 1.2 \times 2 \text{ mm}^3$ .

To evaluate the accuracy of the generated MR-based  $\mu$ -maps, CT-based  $\mu$ -maps were calculated in 511 keV as references of assessment. Ultra-low-dose CT (ULDCT) images of the same volunteers were acquired on the CT module of Discovery 690 VCT PET/CT scanner (GE Healthcare Technologies, WI, USA) with no gantry tilt, tube voltage of 80 kVp and tube current of 10 mA, with 0.5 s rotation time. The voxel size for CT images was  $0.41 \times 0.41 \times 5 \text{ mm}^3$ . The ULDCT protocol, approved by the Ethical Committee of the local institution, was carried out to ensure the total effective dose received by normal volunteers to be in the safe range, in

**Table 1.** Short TE-MR imaging parameters

Parameter	Definition	1.5 T
<i>TE (ms)</i>	Time of echo	1.1
<i>TR (ms)</i>	Repetition time	12
<i>Flip angle</i>		18°
<i>Voxel size (mm)</i>		$1.2 \times 1.2 \times 2$
<i>FOV (mm<sup>2</sup>)</i>	Field of view	$320 \times 320$
<i>Duration (min)</i>	Total acquisition time	7:42

The indices within the parantheses indicate the SI units of each parameter.

compatibility with the International Commission on Radiation Protection (ICRP) report. The total effective dose in this protocol was about 0.4 % of that of a typical CT examination [14].

### MR-Based $\mu$ -Map Generation

The three-class  $\mu$ -maps including air, bone, and soft tissue were derived from STE-MR images in stepwise manner, as summarized in Fig. 1 and explained in details below. All procedures were implemented in MATLAB 2013a (MathWoks, Natick, MA).

### STE-MR Image Pre-processing

MR images were initially masked by applying ‘‘Chan-Vese’’ active contour segmentation approach to isolate unnecessary background information from head regions. In STE-MR images, the unnecessary background information includes background noise. This pre-processing step is mandatory for accurate convergence of level-set contours. Afterwards, the images were denoised employing anisotropic diffusion filtering with optimized parameters to eliminate noise effects while maintaining spatial resolution and edge information.

### Joint Intensity Inhomogeneity Correction and Segmentation Framework

Intensity inhomogeneity is a corrupting artifact, which occurs in MR images as a result of multiple factors, such as non-uniformity of B0 or B1 magnetic fields, or patient anatomy and position [19]. This artifact could significantly complicate the performance of image processing algorithms; particularly, segmentation results become deteriorated where intensity inhomogeneity induces overlapping intensity ranges in the regions to be segmented. Inhomogeneity correction becomes essentially critical in STE-MR image segmentation, in the sense that in these images, air/bone interfaces

in the nasal areas produce susceptibility or inhomogeneity artifact, and consequently accurate separation of these two tissues becomes a challenge.

Spatial intensity inhomogeneity correction from MR images is difficult, as it varies with acquisition parameters, between different subjects and even among various slices of the same subject. Most of the widely used segmentation approaches in medical applications rely on the assumption of image homogeneity [20, 21], which compromises application of these methods in clinical MR image segmentation.

To overcome this issue, here, we exploit a three-phase region-based local level-set segmentation approach proposed and implemented by Li et al. [22] which incorporates intensity inhomogeneity correction with the level-set algorithm. This technique is inherited from the idea that while an accurate segmentation outcome is dependent on inhomogeneity removal, an efficient segmentation algorithm could be employed interactively for estimating the intensity inhomogeneity artifact during segmentation procedure [23–25]. In this technique, k-means clustering is applied to estimate the intensity properties of each region for bias field correction simultaneously with the level-set segmentation. The details of this level-set implementation can be found in [22] and provided in [Supplementary Material](#).

This algorithm incorporates both intensity and spatial information to define continuous boundaries. In order to estimate the clusters over the iterations of level-set evolution, a window or kernel function is applied, which constructs a local clustering criterion as a basis for level-set formulation. The choice of the kernel function is flexible. Here, the Gaussian kernel is employed as the optimal function, which can be specified by a standard deviation of ‘‘ $\sigma$ ’’ and a neighborhood radius of ‘‘ $\rho$ ’’ (Eq. 1).

$$K(u) = \begin{cases} \frac{1}{a} e^{-|u|^2/2\sigma^2}, & \text{for } |u| \leq \rho \\ 0, & \text{otherwise} \end{cases} \quad (1)$$

where  $a$  is a normalization factor, in a way that  $\int K(u) = 1$ . The neighborhood radius is specified with  $\rho = 4\sigma + 1$ .

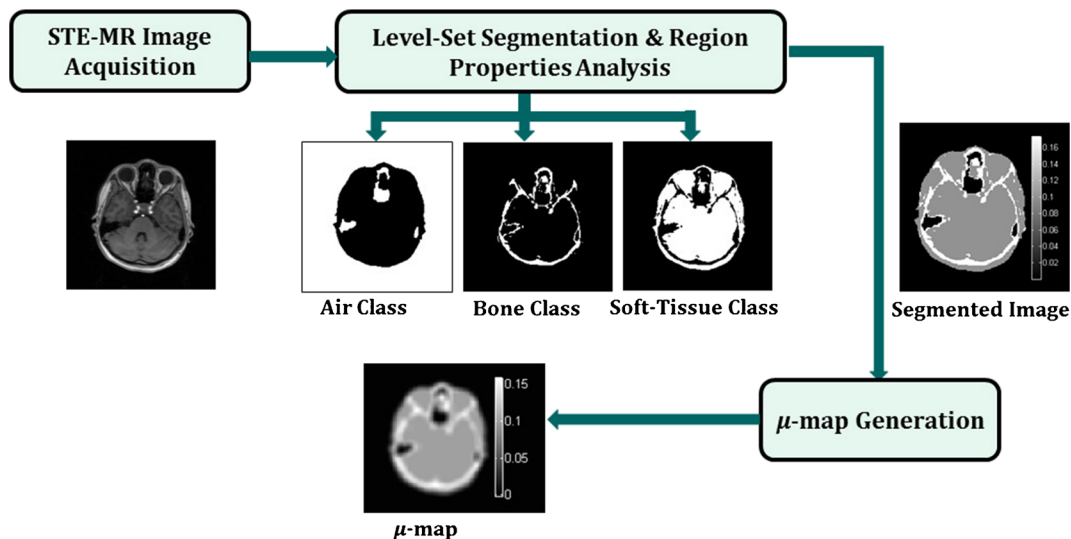


**Fig. 1** The overall segmentation and  $\mu$ -map construction procedure: the STE-MR image is segmented using clustering-based level-set algorithm along with intensity inhomogeneity correction, followed by some region property analysis methods to remove the eye parts, and finally filtering and down-sampling for  $\mu$ -map generation.

For accurate delineation of the air, bone, and soft tissue, the algorithm is applied in two phases: (Phase I) Large amount of  $\sigma$  is selected for the separation of air region;; (Phase II) Small amount of  $\sigma$  is chosen for isolation of bone from soft tissue regions, excluding the air class from phase I.

As the method is region and intensity-based, eye regions with image intensities close to bone signal intensity were misclassified in the bone class. To eliminate these regions, we applied a morphological operator, called shape factor or circularity as a measure of compactness of a shape (Eq. 2):

$$\text{Circularity} = \frac{4\pi A}{P^2} \quad (2)$$

where  $A$  and  $P$  respectively denote the shape area and perimeter [26]. No additional morphological operations were applied for dilating the bone class.

### Derivation of MR-Based $\mu$ -Maps

After completion of STE-MR image segmentation for creation of three image classes, including air, bone, and soft tissue, relevant attenuation coefficients in 511 keV were assigned to each of the classes, based on ICRU Report no. 44 (<http://www.icru.org/home/reports/tissue-substitutes-in-radiation-dosimetry-and-measurement-report-44>). Accordingly, the bone, soft tissue, and air structures were respectively assigned the values of 0.174, 0.99, and 0.00 ( $\text{cm}^{-1}$ ). To generate the  $\mu$ -maps compatible with resolution of Discovery 690 PET/CT scanners (GE Healthcare Technologies, WI, USA), the resulting images were down-sampled to  $128 \times 128$  matrix size and smoothed using a Gaussian filter with a full-width at half-maximum of 6 mm.

### CT-Based $\mu$ -Map Generation

*CT Image Pre-processing* The acquired CT images were masked using ‘‘Chan-Vese’’ active contour model, like MR images, to exclude head region from unwanted areas, including background noise and the bed which need to be excluded to reach accurate registration with STE-MR images and precise segmentation. Afterwards, CT images were co-registered with their corresponding STE-MR images using FLIRT 3D registration method package (<http://fsl.fmrib.ox.ac.uk/fsl/flslwiki/FLIRT>), with affine transformation model and normalized mutual information similarity measure.

### CT Image Segmentation

As it is apparent from the comparison of the voxel sizes of STE-MR and CT images, the slice thickness of CT images is larger than that of STE-MR images, while axial spatial resolution of STE-MR images is lower than CT images. Accordingly and considering reduced sensitivity of ULDCCT images, the commonly used threshold-based segmentation methods [14, 27] do not return reliable discrimination of air/bone/soft tissue classes. Therefore, to overcome the limitations imposed by low-dose CT protocol, we applied a fuzzy C-means clustering approach, as proposed in [28, 29], to differentiate three classes of air, bone, and soft tissue regions (Fig. 2a).

### Validation

For each patient, 20 slices with three slices apart were analyzed and evaluated. We assessed the accuracy of the proposed combined STE-MR imaging and automatic segmentation approach by comparing the segmentation results with CT images of the same subject. Evaluation was performed for each of the region classes, i.e., air, bone, and soft tissue, by considering CT-based segmentation as the gold standard. Voxel-wise comparison of MR- and CT-based segmentation results was performed and true positive (TP), true negative (TN), false positive (FP), and false negative (FN) values were calculated to generate quantitative evaluation metrics, namely sensitivity, specificity, and accuracy. The formulations of these metrics can be found elsewhere [14].

Further assessment of MR- and CT-derived  $\mu$ -maps was carried out by computing their histograms and calculating several histogram features representing different properties of the generated maps. These parameters include mean image intensity, standard deviation of image histogram representing average contrast, normalized variance denoting image smoothness, third moment representing skewness, image energy indicating image uniformity, and image entropy representing randomness of image pixels (Table 2).

## Results

We have applied our proposed framework on STE-MR images of five normal volunteers. By trial and error, for air segmentation, the parameter  $\sigma$  in Eq. 1 is set to 8, and for bone and soft tissue segmentation it is set to 1.5. Fig. 2 illustrates the results of joint clustering-based level-set segmentation and intensity inhomogeneity correction on three sample slices of a normal subject. The slices are chosen from lower third (including sinus area and through the eye sockets), middle third (including part of sinus area and eye sockets), and upper third of the whole-brain STE-MR images, to assess the capability of the algorithm in handling segmentation of several brain regions. The lower third slice contains complex bone structures, which is a challenging region for most of the image segmentation algorithms. For visual inspection of the segmentation results, in Fig. 2, CT images are presented in column *a* where their corresponding segmented images are illustrated in column *c*. Column *b* depicts the relative STE-MR images with segmented results indicated in column *d*. For segmented images in columns *c* and *d*, soft tissue is coded with gray, cortical bone with white, and air with black. The MR-derived  $\mu$ -map of the corresponding slice can be observed in column *e*.

Quantitative assessment of segmentation outcomes was carried out on a voxel-by-voxel basis between segmented STE-MR and CT images. The quantitative evaluation outcome in terms of sensitivity, specificity, and accuracy metrics for the three classes of cortical bone, air, and soft tissue regions is summarized in Table 3. A large majority of voxels were correctly attributed to their expected tissue

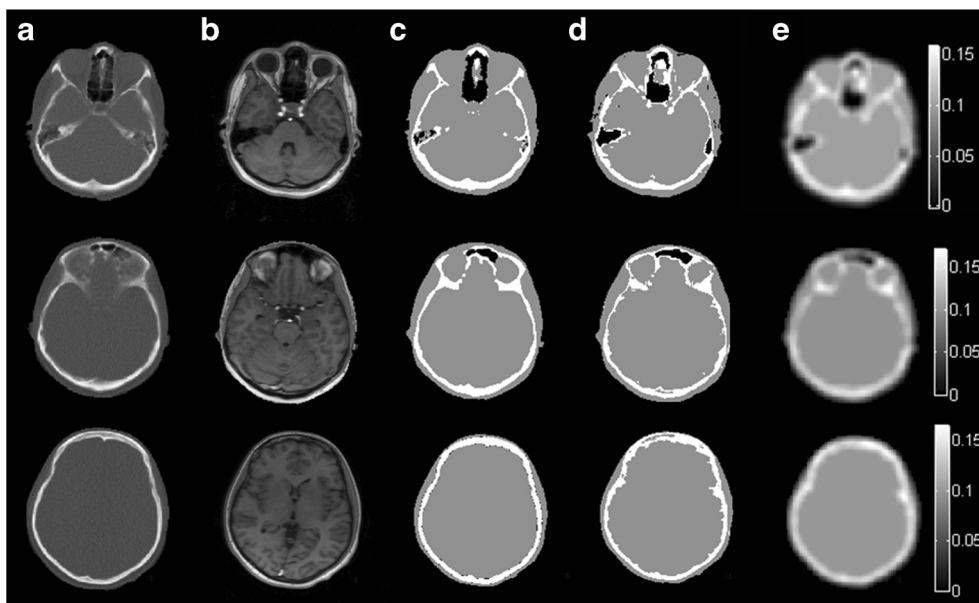


**Fig. 2** Illustration of the results of the proposed segmentation approach on three sample slices of STE-MR images of a normal subject: (*first row*) lower third, (*second row*) middle third, and (*last row*) upper third slices of a whole-brain image. **a** CT images; **b** corresponding STE-MR images; **c** segmented STE-MR images classified into three different regions: air (*black*), soft tissue (*gray*), and bone (*white*); **d** segmented CT images classified into the aforementioned three regions; and **e** the derived MR-based  $\mu$ -maps.

class: 90.71 % accuracy for cortical bone, 95.72 % for soft tissue, and 90 % for air.

In Figs. 3 and 4, the differences of segmentation results obtained by CT and STE-MR images and CT- and MR-derived  $\mu$ -maps are respectively represented. These maps are indicated in color-coded format to provide visual comparison of the classified regions. Average differences between the segmented STE-MR images with respect to the segmented CT images were  $0.008 \pm 0.024 \text{ cm}^{-1}$  and among the generated MR- and CT-derived  $\mu$ -maps were  $0.003 \pm 0.005 \text{ cm}^{-1}$ .

Further assessment of classification accuracy was performed by computing the number of voxels in each of the three classes of cortical bone, air, and soft tissue areas assigned to the correct or incorrect classes. Fig. 5 illustrates the true/false assignments of average number of voxels to each of the cortical bone, air, and soft tissue classes.

Additionally, a new evaluation method was employed for investigating the similarities of CT- and MR-based  $\mu$ -maps.

This was performed by accumulating the image intensities within each of CT- or MR-based  $\mu$ -maps derived from the three sample slices represented in Fig. 2. CT- and MR-derived histograms were calculated to more closely probe the similarities of the generated  $\mu$ -maps. Statistical histogram-derived features quantitatively represent probability distribution of the image intensities. As indicated in Fig. 6, the histograms of CT- and MR-derived  $\mu$ -maps are very similar. This was further approved by comparing the quantities of histogram features (Table 4).

## Discussion

The presented work was implemented by adopting the idea of incorporating single STE-MR images of the brain with an automatic clustering-based level-set segmentation technique with simultaneous intensity inhomogeneity correction [22]. As proposed in [14], STE-MR images with the devised protocol can provide sufficient signal-to-noise ratio (SNR) to detect bone signal. By exploiting optimal clinically feasible short echo-time MR acquisition followed by an advanced image segmentation, visualization of cortical bone, and its differentiation from air regions becomes possible. The image processing steps make distinctive contrasts between soft, air, and bone regions. This is important in the context of attenuation correction of PET images, as MR images offer desirable properties such as superb soft tissue contrast, non-ionized acquisition strategy, and multi-parametric imaging within a single acquisition session. Therefore, the capability of detecting cortical bone and its accurate differentiation

**Table 2.** Definitions of histogram features

Feature	Definition
Mean	Average of image histogram
Contrast	Standard deviation of image histogram, i.e., dispersion of the histogram
Smoothness	Normalized variance of image histogram
Skewness	Third moment of image histogram, a measure of asymmetry of the probability distribution
Uniformity	Image energy
Entropy	Irregularities of image pixels

**Table 3.** Quantitative evaluation results of classifying STE-MR images into three classes of cortical bone, air, and soft tissue, by comparing the MR-segmented regions with the corresponding CT-segmented regions. The evaluation is denoted in terms of sensitivity, specificity, and accuracy

Cortical bone			Air			Soft tissue		
Sens. (%)	Spec. (%)	Acc. (%)	Sens. (%)	Spec. (%)	Acc. (%)	Sens. (%)	Spec. (%)	Acc. (%)
74.52	94.54	90.71	87.87	92.15	90.09	93.59	97.02	95.72

from air regions can further convert MRI as the imaging method of choice in the context of PET attenuation correction.

In this work, automatic clustering-based level-set segmentation technique incorporated with intensity inhomogeneity correction on single STE-MRI was applied to

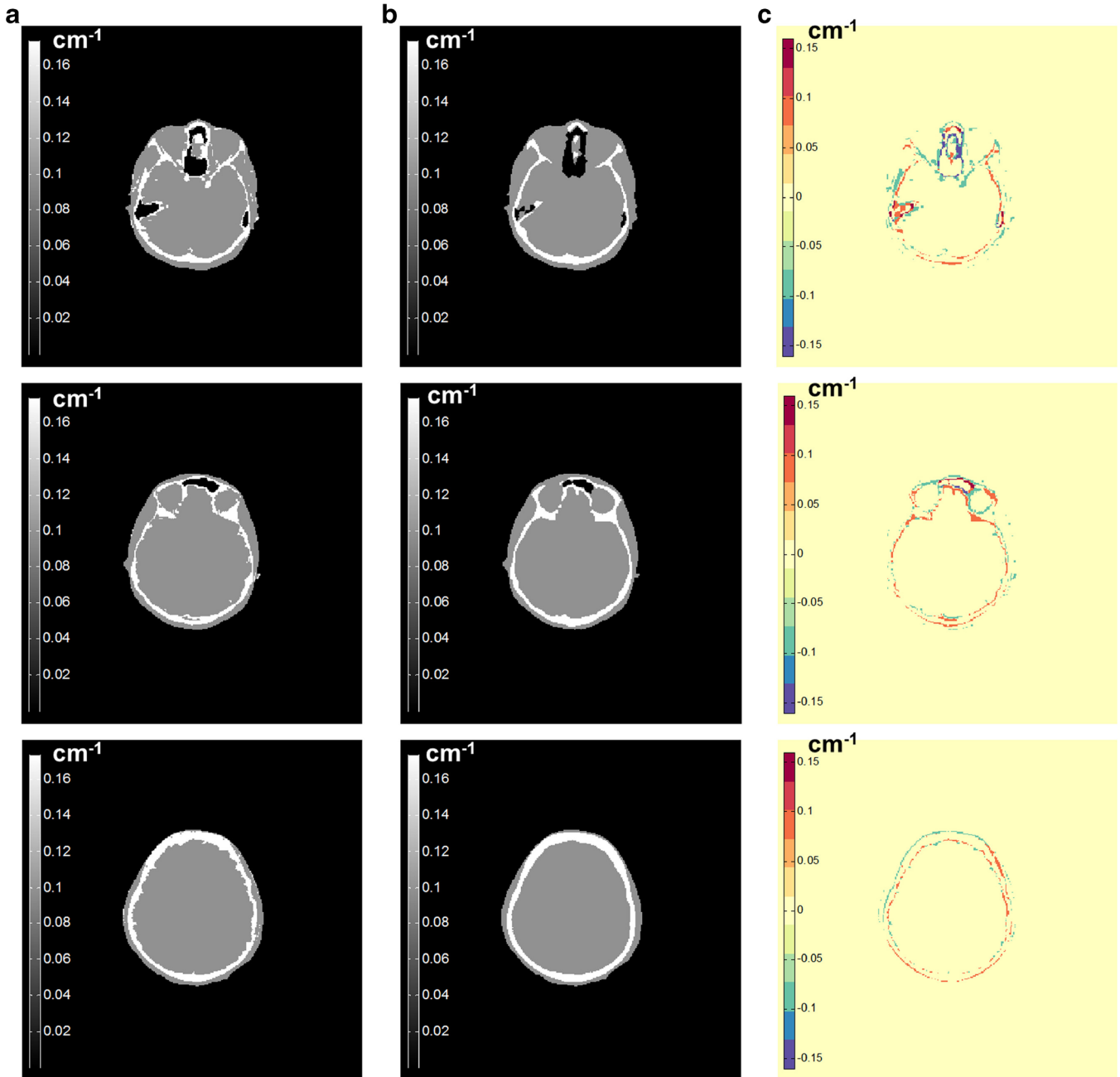


**Fig. 3** Segmentation results generated from **a** STE-MR images and **b** CT images. **c** The difference between segmentation results of CT and STE-MR images for the same slices of Fig. 2. The segmented regions (air, bone, and soft tissue) for MR- and CT-based segmentation images are assigned the related attenuation numbers. The *color bars* in difference maps represent errors of MR-based attenuation maps with respect to the corresponding CT-based attenuation maps.

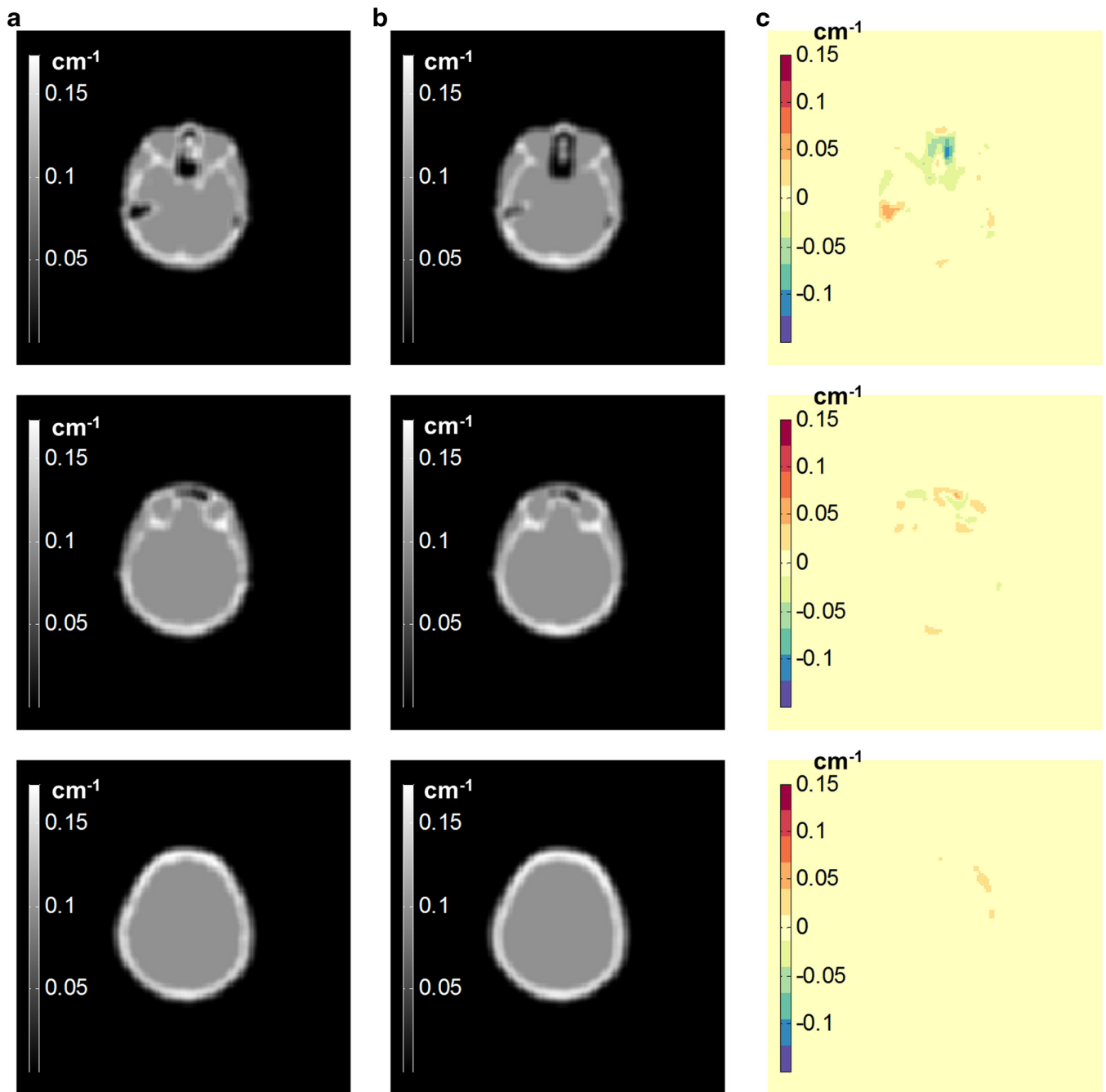


Fig. 4 The  $\mu$ -maps derived from **a** STE-MR images and **b** CT images. **c** The difference between CT- and MR-derived  $\mu$ -maps for the same slices of Fig. 2. The *color bars* in difference maps represent errors of MR-based attenuation maps with respect to the corresponding CT-based attenuation maps.

investigate the competing role of MR-derived with CT-derived  $\mu$ -maps. The proposed combined STE-MR imaging and automatic segmentation approach resulted in accuracy and specificity values of over 90 and 92 % in all regions, respectively, and a sensitivity of 88 % for air, 94 % for the soft tissue, and 74 % for cortical bone region. A recent study by Khateri et al. reported sensitivity of 92 % for air, 95 % for soft tissue, and 75 % for cortical bone [14]. While the results achieved by our proposed method are generally

comparable to those achieved by Khateri et al., we claim that the three-phase level-set segmentation algorithm exploited in our work is straightforward, automatic, and reproducible. This approach neither involves extensive image processing procedures including morphological operators nor requires incorporating several images acquired by STE/Dixon technique followed by subtraction and intersection operations for reaching the final result as in [14]. As we have indicated in Fig. 5, only 4 % of air misclassification belongs to the

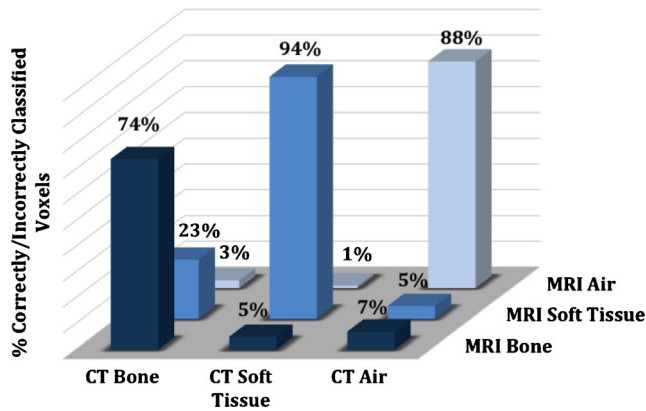


Fig. 5 The diagram representing the percentages of correctly and mistakenly classified voxels.

cortical bone class. About 5 % of air region is misclassified in the soft tissue category, which is a result of employing low spatial resolution ultra-low-dose CT images as a reference of comparison. About 23 % of cortical bone being misclassified as soft tissue and 5 % of soft tissue being categorized as cortical bone is comparable to the achieved results in related works. In the work by Khateri et al., 24 % of cortical bone was assigned to soft tissue and 4 % of soft tissue was misclassified as cortical bone [14], while Keereman et al. reported 25 % of bone having been misclassified as soft tissue and 20 % of soft tissue as bone, employing a UTE-based attenuation correction approach [17].

In a study proposed by An et al., a two-phase region-based level-set segmentation approach has been applied on UTE-MR images of the head incorporated with morphological operators, subtraction, and intersection of two UTE images to achieve classification of air, bone, and soft tissue classes [30]. The accuracy of the segmentation approach has not been directly reported but visual inspection of the results indicates misclassification of bone regions as soft or air regions as well as discontinued cortical bone in few areas. The three-phase level-set method in conjunction with single STE-MR imaging proposed in our work seems to outperform the mentioned study in reducing the computational burden by employing simpler framework as well as imposing less imaging complexity by clinically feasible single STE-MR imaging.

The results suggest that STE-MRI can provide comparable accuracy and reliable agreement with CT images. This approach could also be proposed as an alternation to UTE MR imaging or combined STE/Dixon imaging technique in PET attenuation correction, as it offers feasible properties in the sense that this approach can be applied using a clinically applicable protocol (unlike UTE-MRI [13, 17]) and a single STE image (unlike combined STE/Dixon technique) with comparable accuracy.

This is worth mentioning that we have employed a clinical MR pulse sequence, which can easily be

incorporated in a routine clinical imaging session. This is while application of UTE-MRI in clinics is still a matter of controversy, as its implementation requires complicated hardware. Accordingly, the proposed scheme in this paper could be used as a reliable alternative to UTE-based attenuation correction methods. On a related note, unlike previous works where the accuracy of tissue segmentation has been performed on a selected region of interest [17], we have calculated the accuracy of tissue segmentation on the total slice and yet have achieved close outcomes in tissue segmentation to the mentioned studies.

As it can be observed in the difference maps of STE-MR and CT segmentations and  $\mu$ -maps, ethmoid sinuses exhibit more errors in attenuation correction procedure. This could be majorly attributed to unavoidable susceptibility artifact in MR images in the bone-air interface. Furthermore, existence of fewer bone voxels in these regions causes small variations to induce large changes in sensitivity of cortical bone segmentation. However, ULDC imaging produces images with ambiguous borders between cortical bone and air or soft tissue regions; i.e., the sensitivity of bone detection in ULDC imaging becomes deteriorated and therefore cannot be adopted as the “gold standard” of comparison. This can be inferred by visual inspection of ULDC images and comparison with corresponding STE-MR images as illustrated in Fig. 2 (also confirmed by an expert radiologist). Interestingly, according to the quantitative evaluation results of Fig. 5 (sensitivity of segmented regions), some parts of CT cortical bone regions are attributed to MR soft tissue regions. As MRI provides superior soft tissue contrast in contrast to CT images, this misclassification is due to inaccuracy of ULDC in providing differentiation of bone and soft tissue regions. Therefore, the raised error in discrimination of cortical bone from proximal air or soft tissue regions is partly due to reduced sensitivity of ULDC images, being employed as standard of comparison for STE-MR imaging. Nonetheless, this imaging is the best evaluation standard which can be employed when normal volunteers are being investigated.

This problem becomes less severe after generating  $\mu$ -maps, as the resulting  $\mu$ -maps are constructed by down-sampling and applying smoothing filter to the segmented images, and therefore, the differences among CT- and MR-based  $\mu$ -maps significantly reduce and their similarities increase. This inquiry was approved by computing histograms of CT- and MR-derived  $\mu$ -maps (Fig. 6) and indicating that the  $\mu$ -maps are very similar in the spatial distribution of image intensities. This was further confirmed by quantitative assessment presented in Table 4. The proximity of the histogram means and standard deviation (contrast) of the two  $\mu$ -maps is representative of their similar distribution over the range of image intensities. Similar values of normalized variance of the two histograms demonstrate that the two  $\mu$ -maps have almost equally smoothed distributions. Interrogation of skewness, energy,

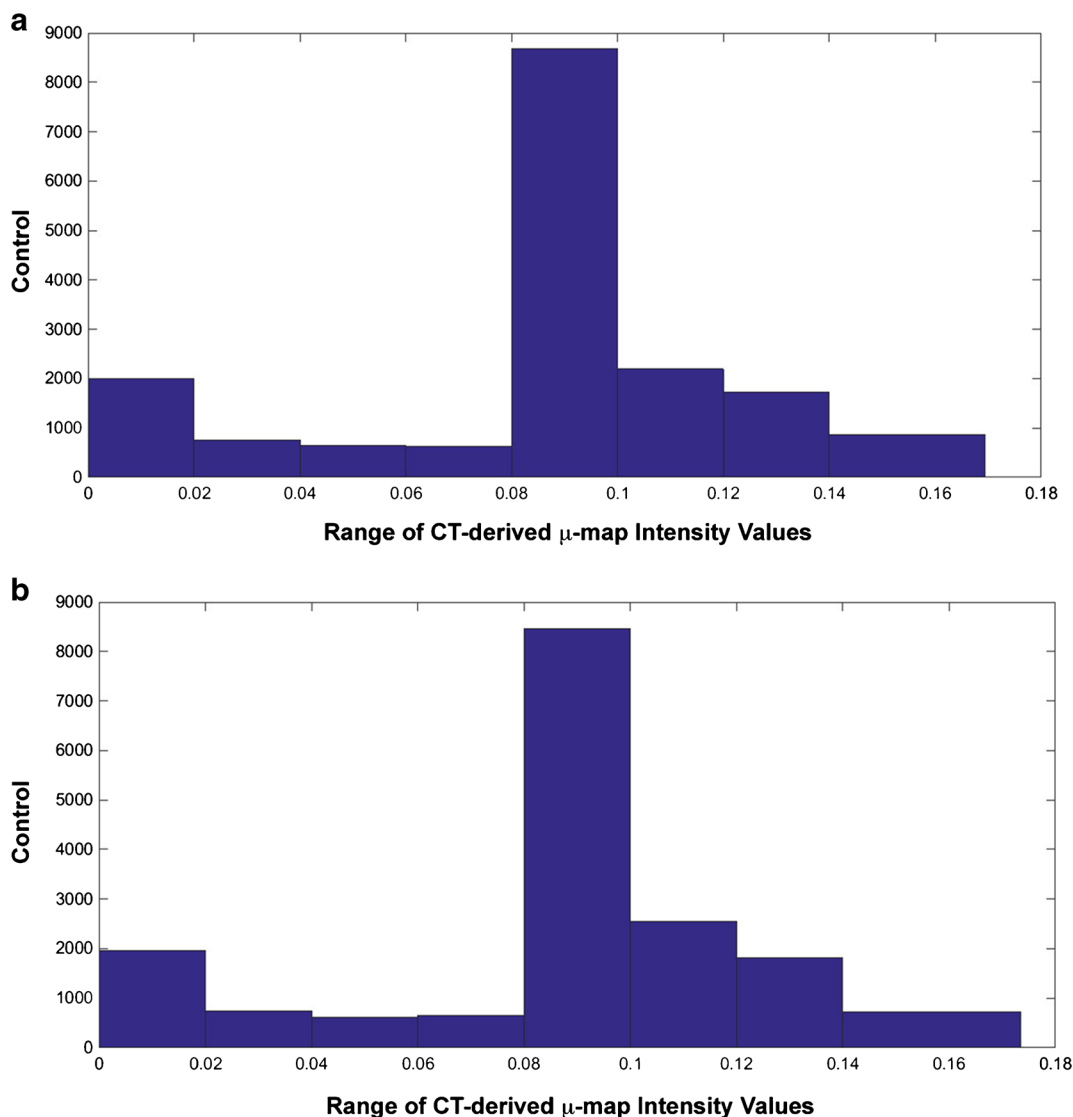


Fig. 6 Histograms of **a** CT- and **b** MR-based  $\mu$ -maps, where the intensity values of CT-/MR-based  $\mu$ -maps are accumulated to represent an overall histogram.

and entropy features in the two  $\mu$ -maps indicates equal symmetry, homogeneity (uniformity), and degree of irregularities of image intensities in both histograms which further confirms that the two histogram shapes are closely equal and can be employed interchangeably.

Nonetheless, some limitations of this study should be outlined here. First, this work was a pilot study performed with small study subjects. Therefore, to generalize this method, it is essential to validate it on more subjects and patients. Second, to follow regulations of the report by

International Commission on Radiation Protection (ICRP) about the safe CT dose range for normal volunteers, ULDCT images were acquired and inevitably, low spatial resolution of ULDCT images with unclear borders between bone and soft tissues may have contributed to suboptimal sensitivity of bone discrimination. In our future works including patients, this validation can be more confidently performed using high-resolution CT images acquired as the standard pre-surgical imaging protocol for patients undergoing head surgeries.

Table 4. Quantitative values of histogram features of MR- and CT-derived  $\mu$ -maps

	Mean	Contrast	Smoothness	Skewness	Uniformity	Entropy
MR-derived $\mu$ -map	4.06	9.72	0.00145	0.030	0.7021	1.215
CT-derived $\mu$ -map	4.07	9.79	0.00147	0.031	0.7028	1.210

## Conclusion

Accurate segmentation of air-bone interface has a major impact on MRI-based attenuation correction of PET images and consequently on achieving meaningful qualitative and quantitative PET image interpretation [10]. In the presented work, it was shown that the challenging task of air and bone discrimination, which becomes further complicated by MRI field inhomogeneity, can be resolved in a unified level-set segmentation and intensity inhomogeneity correction scheme on a single clinical MR pulse sequence, the so-called short-TE (STE) imaging method. This approach can reliably discriminate bony structures from the proximal air and soft tissue in STE-MR images, which is suitable for generating MR-based  $\mu$ -maps.

**Compliance with Ethical Standards.** Study approval was obtained from the Medical Ethics Committee of Tehran University of Medical Sciences (License number 1432), and the subjects were included if they provided written informed consent.

### Ethical Approval

All procedures performed in this study involving human participants were in accordance with the ethical standards of the Tehran University of Medical Sciences research committee with the Ethics License Number 1432.

### Conflict of Interest

The authors declare that they have no conflict of interest.

## References

- Zaidi H, Montandon M-L, Slosman DO (2004) Attenuation compensation in cerebral 3D PET: effect of the attenuation map on absolute and relative quantitation. *Eur Journal Nucl Med Mol Imaging* 31:52–63
- Zaidi H, Del Guerra A (2011) An outlook on future design of hybrid PET/MRI systems. *Med Phys* 38:5667–5689
- Zaidi H (2007) Is MR-guided attenuation correction a viable option for dual-modality PET/MR imaging? 1. *Radiology* 244:639–642
- Pichler BJ, Wehrl HF, Kolb A, Judenhofer MS (2008) Positron emission tomography/magnetic resonance imaging: the next generation of multimodality imaging? *Semin Nucl Med* 38:199–208P
- Schlemmer H-PW, Pichler BJ, Schmand M et al (2008) Simultaneous MR/PET imaging of the human brain: feasibility study 1. *Radiology* 248:1028–1035
- Wagenknecht G, Kaiser H-J, Mottaghy FM, Herzog H (2013) MRI for attenuation correction in PET: methods and challenges. *Magn Reson Mater Phys Biol Med* 26:99–113
- Keereman V, Mollet P, Berker Y et al (2013) Challenges and current methods for attenuation correction in PET/MR. *Magn Reson Mater Phys Biol Med* 26:81–98
- Navalpakkam BK, Braun H, Kuwert T, Quick HH (2013) Magnetic resonance-based attenuation correction for PET/MR hybrid imaging using continuous valued attenuation maps. *Invest Radiol* 48:323–332
- Hofmann M, Pichler B, Schölkopf B, Beyer T (2009) Towards quantitative PET/MRI: a review of MR-based attenuation correction techniques. *Eur Journal Nucl Med Mol Imaging* 36:93–104
- Akbarzadeh A, Ay MR, Ahmadian A et al (2013) MRI-guided attenuation correction in whole-body PET/MR: assessment of the effect of bone attenuation. *Ann Nucl Med* 27:152–162
- Kops ER, Herzog H (2008) Template based attenuation correction for PET in MR-PET scanners. In: 2008 IEEE Nuclear Science Symposium Conference Record, IEEE, Dresden, Germany, pp 3786–3789
- Malone IB, Ansorge RE, Williams GB et al (2011) Attenuation correction methods suitable for brain imaging with a PET/MRI scanner: a comparison of tissue atlas and template attenuation map approaches. *J Nucl Med* 52:1142–1149
- Catana C, van der Kouwe A, Benner T et al (2010) Toward implementing an MRI-based PET attenuation-correction method for neurologic studies on the MR-PET brain prototype. *J Nucl Med* 51:1431–1438
- Khateri P, Rad HS, Jafari AH et al (2015) Generation of a four-class attenuation Map for MRI-based attenuation correction of PET data in the head area using a novel combination of STE/Dixon-MRI and FCM clustering. *Mol Imaging Biol* 17:884–892
- Hofmann M, Steinke F, Scheel V et al (2008) MRI-based attenuation correction for PET/MRI: a novel approach combining pattern recognition and atlas registration. *J Nucl Med* 49:1875–1883
- Reza Ay M, Akbarzadeh A, Ahmadian A, Zaidi H (2014) Classification of bones from MR images in torso PET-MR imaging using a statistical shape model. *Nucl Instrum Meth A* 734:196–200
- Keereman V, Fierens Y, Broux T et al (2010) MRI-based attenuation correction for PET/MRI using ultrashort echo time sequences. *J Nucl Med* 51:812–818
- Khateri P, Rad HS, Fathi A, Ay MR (2013) Generation of attenuation map for MR-based attenuation correction of PET data in the head area employing 3D short echo time MR imaging. *Nucl Instrum Meth A* 702:133–136
- Kazerooni AF, Ahmadian A, Saberi H, Alirezaie J, Rad HS (2012) An efficient algorithm for registration of pre-and intra-operative brain MRI images to correct intensity inhomogeneity. In: Information Science, Signal Processing and their Applications (ISSPA), 2012 11th International Conference, IEEE, Montreal, Canada, pp 253–258
- Chan TF, Vese LA (2001) Active contours without edges. *IEEE Trans Image Process* 10:266–277
- Ronfard R (1994) Region-based strategies for active contour models. *Int J Comput Vision* 13:229–251
- Li C, Huang R, Ding Z, Gatenby J, Metaxas DN, Gore JC (2011) A level set method for image segmentation in the presence of intensity inhomogeneities with application to MRI. *IEEE Trans Image Process* 20:2007–2016
- Van Leemput K, Maes F, Vandermeulen D, Suetens P (1999) Automated model-based bias field correction of MR images of the brain. *IEEE Trans Med Imaging* 18:885–896
- Kazerooni AF, Aarabi MH, Ay M, Rad HS (2014) A fully automated and reproducible level-set segmentation approach for generation of MR-based attenuation correction map of PET images in the brain employing single STE-MR imaging modality. *EJNMMI Physics* 1:1–2
- Aarabi MH, Kazerooni AF, Khateri P, Ay MR, Rad HS (2014) A robust MR-based attenuation map generation in short-TE MR images of the head employing hybrid spatial fuzzy C-means clustering and intensity inhomogeneity correction. *EJNMMI Physics* 1:1–2
- Kazerooni AF, A'arabi MH, Ay M, Rad HS (2015) Generation of MR-based attenuation correction map of PET images in the brain employing joint segmentation of skull and soft-tissue from single short-TE MR imaging modality. In *Computational Methods for Molecular Imaging*. Springer, Switzerland 22: 139–147
- Keereman V (2011) MRI-based attenuation correction for emission tomography. Ghent University, Ghent
- Mohamed NA, Ahmed MN, Farag A (1999) Modified fuzzy c-mean in medical image segmentation [abstract]. *Engin Med* 6:3429–3432P
- Hu Q, Qian G, Aziz A, & Nowinski WL (2006) Segmentation of brain from computed tomography head images. In: 2005 IEEE Engineering in Medicine and Biology 27th Annual Conference, IEEE, Shanghai, China, pp 3375–3378
- An HJ, Seo S, Kang H, Choi H, Cheon GJ, Kim HJ (2016) MRI-based attenuation correction for PET/MRI using multiphase level-set method. *J Nucl Med* 57(4):587–593